Opto-Electronic Technology

CN 51-1811/O4 ISSN (Print) 2097-6003 ISSN (Online) 2097-8006

Short-chain ligand engineering toward room-temperature synthesis of high-brightness $CsPbBr_3$ nanocrystals for color-conversion LED applications

Xiaochen Fang, Zengxian Tang, Ronggan Lu, Guixiang Ding, Xiaotong Zhang, Yongfeng Liu, Qingyu Xie, Yihong Dong, Dongdong Yan*, Hao Xie*, Xiaoyu Wang and Weixiang Ye*

Citation: Fang XC, Tang ZX, Lu RG et al. Short-chain ligand engineering toward room-temperature synthesis of high-brightness $CsPbBr_3$ nanocrystals for color-conversion LED applications. *Opto-Electron Technol* **3**, 260024 (2027).

https://doi.org/10.29026/oet.2026.260024

Received: 17 June 2026; Accepted: 17 September 2026; Published online: 31 October 2026

Related articles

Overcoming challenges in InP-based quantum dots: from nucleation mechanisms to high-performance quantum dot light-emitting diodes

Yangyang Bian, Qian Li, Fei Chen, et al

Opto-Electronic Advances 2026, **9**(3): 250270 doi: 10.29026/oea.2026.250270

Highly sensitive DUV-SWIR photodetectors by natural flavonoid-derivative isomers through a multisite chelation strategy

Nan Ding, Donggang Li, Mingyu Yao, et al

Opto-Electronic Science 2026, **5**(6): 260014 doi: 10.29026/oes.2026.260014

Recent advances in exciton-polariton in perovskite

Khalil As'ham, Andergachew Mekonnen Berhe, Ibrahim A. M. Al-Ani, et al

Opto-Electronic Science 2025, **4**(9): 250001 doi: 10.29026/oes.2025.250001

Dual quasi-BIC resonances synergized laser cooling in halide perovskite metasurface

Ying Che, Peng Lu, Yang Li, et al

Opto-Electronic Technology 2026, **2**(1): 250013 doi: 10.29026/oet.2026.250013

More related articles in Opto-Electronic Journals Group website

Opto-Electronic Journals Group

https://www.oejournal.org

OE_Journal @OptoElectronAdv

This is an early view version and will be formally published in a coming issue with other articles in due time.

OET | Opto-Electronic Technology

Article

2027, Vol. , No.

Open Access

Short-chain ligand engineering toward room-temperature synthesis of high-brightness $CsPbBr_3$ nanocrystals for color-conversion LED applications

Xiaochen Fang[1†], Zengxian Tang[1†], Ronggan Lu[1†], Guixiang Ding[2], Xiaotong Zhang[2], Yongfeng Liu[3], Qingyu Xie[3], Yihong Dong[1], Dongdong Yan[1*], Hao Xie[1*], Xiaoyu Wang[1] and Weixiang Ye[1*]

Abstract: The labile nature of conventional long-chain ligands on $CsPbBr_3$ quantum dots (QDs) often leads to desorption during device fabrication, creating surface traps that compromise efficiency and stability. Here, we employ a supersaturation-precipitation method at room temperature, introducing 4-bromobutyric acid (BA) as a short-chain co-ligand alongside conventional oleic acid (OA) and oleylamine (OAm). The BA ligand anchors to surface Pb^{2+} via its carboxyl group, while its terminal Br^- effectively fills surface Br vacancies. The combination of BA and OA enhances the photoluminescence quantum yield (PLQY) to 84.96% and improves stability. density functional theory (DFT) calculations were performed on $CsPbBr_3$-OA, $CsPbBr_3$-BA and $CsPbBr_3$-OA/BA QDs to analyze charge density difference, density of states, and binding energy, demonstrating that BA can passivate surface defects, thereby enhancing the stability and photoluminescence (PL) performance of the materials. Single-particle spectroscopy shows that BA ligand engineering narrows the emission linewidth and prolongs the dephasing time of $CsPbBr_3$ QDs, evidencing reduced local disorder and enhanced excitonic coherence. Coupled with a commercial 365 nm UV chip, green LED based on $CsPbBr_3$-OA/BA QDs emits 1.42 times the PL intensity of $CsPbBr_3$-OA 's LED at 2.7 V. This work establishes short-chain ligands as an effective strategy to simultaneously achieve high efficiency and operational stability in perovskite QDs optoelectronics.

Keywords: 4-bromobutyric acid; stability; green LED; ligand engineering

DOI: 10.29026/oet.2026.260024 | CSTR: 32419.14.oet.2026.260024

Citation: Fang XC, Tang ZX, Lu RG et al. Short-chain ligand engineering toward room-temperature synthesis of high-brightness $CsPbBr_3$ nanocrystals for color-conversion LED applications. *Opto-Electron Technol*, 260024 (2027).

1 Introduction

Metal-halide perovskite quantum dots (QDs) have attracted intense interest for optoelectronic applications because of their large light-absorption coefficients, narrowband emission with high color purity, and high photoluminescence quantum yield (PLQY)[1–4]. However, their practical deployment remains limited by rapid degradation under air, light, and elevated temperature, which is widely associated with the highly dynamic binding of conventional ligands to ionic QDs surfaces and the ensuing ligand desorption[5–8]. This ligand loss progressively generates surface traps, accelerates surface reconstruction in polar environments, and ultimately deteriorates both optical and electronic properties[9]. Among the $CsPbX_3$ (X=Cl, Br and I) family, $CsPbBr_3$ QDs serve as a representative model system with prototypical surface chemistry and broad relevance to lighting and display applications. OA interacts dynamically with $CsPbBr_3$ QDs through hydrogen bonding with surface halides and yet such labile interactions render the surface particularly vulnerable to etching and partial dissolution in polar media, causing colloidal $CsPbBr_3$ QDs instability and fast PL decay[10]. While such interactions facilitate nucleation and

Received: 17 June 2026

Accepted: 17 September 2026

Published online: 31 October 2026

[1]School of Physics and Optoelectronic Engineering, Hainan University, Haikou 570228, China; [2]College of Materials Engineering, Fujian Agriculture and Forestry University, Fuzhou 350002, China; [3]College of Physical Science and Technology & Microelectronics Industry Research Institute, Yangzhou University, Yangzhou 225002, China.

†These authors contributed equally to this work.

*Correspondence: DD Yan, E-mail: ddyan@hainanu.edu.cn; H Xie, E-mail: xiehao@hainanu.edu.cn; WX Ye, E-mail: wxy@hainanu.edu.cn

This is an early view version and will be formally published in a coming issue with other articles in due time.

growth, they also reflect the intrinsically ionic and labile nature of perovskite QDs surfaces. Therefore, developing a ligand shell that is both strongly anchored and densely packed is imperative for realizing the full potential of $CsPbBr_3$ QDs[11].

Ligand engineering employing multidentate chelators and ionic surfactants is an effective strategy to strengthen surface passivation and suppress ion migration. A wide range of ligand strategies has been explored to stabilize perovskite QDs, among which surface-ligand engineering has proven particularly effective in preserving colloidal integrity and enhancing stability[12–14]. For example, Zeng et al. reported that a multidentate amine chelating ligand, N'-(2-aminoethyl)-N'-hexadecylethane-1,2-diamine (AHDA), effectively passivates $CsPbI_3$ QDs; the protonated AHDA binds strongly to the perovskite surface with a calculated binding energy of 2.36 eV, exceeding that of typical ammonium ligands (1.47 eV)[15]. However, it requires a stronger acid (BTMPA, bis(2,4,4-trimethylpentyl) phosphinic acid) to fully protonate AHDA (N'-(2-aminoethyl)-N'-hexadecylethane-1,2-diamine). Akash et al. employed sodium dodecyl sulfate (SDS) to modify $CsPbBr_{1.5}I_{1.5}$ QDs, achieving enhanced environmental stability and PL efficiency through dual passivation of uncoordinated Pb sites and halide defects, thereby suppressing halide migration and preventing phase segregation[16]. Although SDS can suppress phase segregation in perovskite QDs to some extent, it does not significantly improve the stability of their PL emission. Collectively, these studies highlight the promise of ligand-mediated surface engineering to improve stability and optoelectronic performance. Simultaneously achieving high PLQY, robust surface passivation, and long-term stability remains challenging. In particular, weakly bound long-chain ligands can dynamically desorb from the QDs surface, leading to the formation of surface defects and degradation of the optical properties under environmental or operational stress. Therefore, rational regulation of ligand–surface interactions is essential for improving both the luminescence efficiency and robustness of $CsPbBr_3$ QDs. In this study, BA provides a useful complementary ligand to conventional OA because its shorter molecular chain and carboxyl functional group can modify the local coordination environment of surface Pb^{2+} sites while reducing the steric constraints associated with long-chain ligands. Such a mixed-ligand strategy may therefore provide a more balanced surface-passivation environment than the use of OA alone[17]. This consideration is particularly relevant for $CsPbBr_3$ QDs synthesized through room-temperature supersaturation recrystallization, which offers a simple and mild alternative to conventional high-temperature synthetic routes but places greater demands on effective surface stabilization[18–21]. In this work, we synthesized $CsPbBr_3$ QDs at room temperature under ambient conditions through a supersaturation recrystallization route, using conventional ligands OA and OAm in combination with short-chain carboxylic acid 4-bromobutyric acid (BA). We hypothesize that introducing a short-chain acid can increase surface packing density (mitigating steric hindrance) while a properly tuned acid-to-amine equilibrium stabilizes the ligand shell, thereby simultaneously reducing surface traps and resisting polar attack. Systematic variation of the acid-to-amine ratio revealed that a 3:1 proportion, combined with equimolar BA and OA, maximized surface-defect passivation and resulted in the highest PLQY of 84.96 %. To directly probe excitonic coherence at the single-particle level, we further implemented dark-field spectral microscopy to resolve the emission linewidth and extract the dephasing time, providing a sensitive metric for ligand-induced suppression of local environmental fluctuations. The resulting hydrophobic ligand shell, stabilized primarily by BA and further reinforced by OA, markedly enhances both chemical stability and photostability under water exposure, elevated temperature, and ultraviolet irradiation. When incorporated into a phosphor-converted light-emitting diode (LED), these $CsPbBr_3$-BA/OA QDs deliver an external quantum efficiency of 2.25 %, demonstrating a scalable route that bridges high-quality emission with ambient-compatible processing.

2 Results and discussion

Given that the conventional OA and OAm ligand shell on $CsPbBr_3$ QDs is highly dynamic and prone to desorption, we introduce BA as a short-chain carboxylic acid co-ligand with OA to reinforce ligand anchoring while improving surface coverage. To rationalize this ligand selection, we evaluated the ligand induced charge redistribution at the $CsPbBr_3$ surface. To elucidate how BA and OA regulate the surface electronic structure of $CsPbBr_3$ QDs, we performed density functional theory (DFT) calculations to map the charge density difference upon ligand adsorption. Figure S1 presents the six models constructed in this calculation, including three configurations of $CsPbBr_3$-OA, $CsPbBr_3$-BA, and $CsPbBr_3$-OA/BA (Fig. S1(a–c)) and three configurations of $CsPbBr_3$-OA, $CsPbBr_3$-BA, and $CsPbBr_3$-OA/BA with Br vacancies and with Br vacancies repaired by BA. Figure S2 first shows the charge-density difference of bare $CsPbBr_3$ QDs, where blue and yellow represent electron accumulation depletion, respectively. We then evaluated the ligand-induced redistribution for $CsPbBr_3$ capped with OA and BA, and their combination. As shown in Fig. 1(a–c), BA induces a more pronounced charge rearrangement around surface Pb^{2+} sites than OA, consistent with stronger ligand surface interaction. In accordance with this trend, the calculated binding energies in the $CsPbBr_3$ OA and BA co-adsorption model are −8.38 eV for BA and −7.93 eV for OA (Fig. 1(c)), indicating that BA binds more favorably to the QDs surface. Together, these results support that incorporating BA can stabilize the ligand shell and thus provide a more robust surface passivation for $CsPbBr_3$ QDs.

To further elucidate how ligand chemistry modulates the

This is an early view version and will be formally published in a coming issue with other articles in due time.

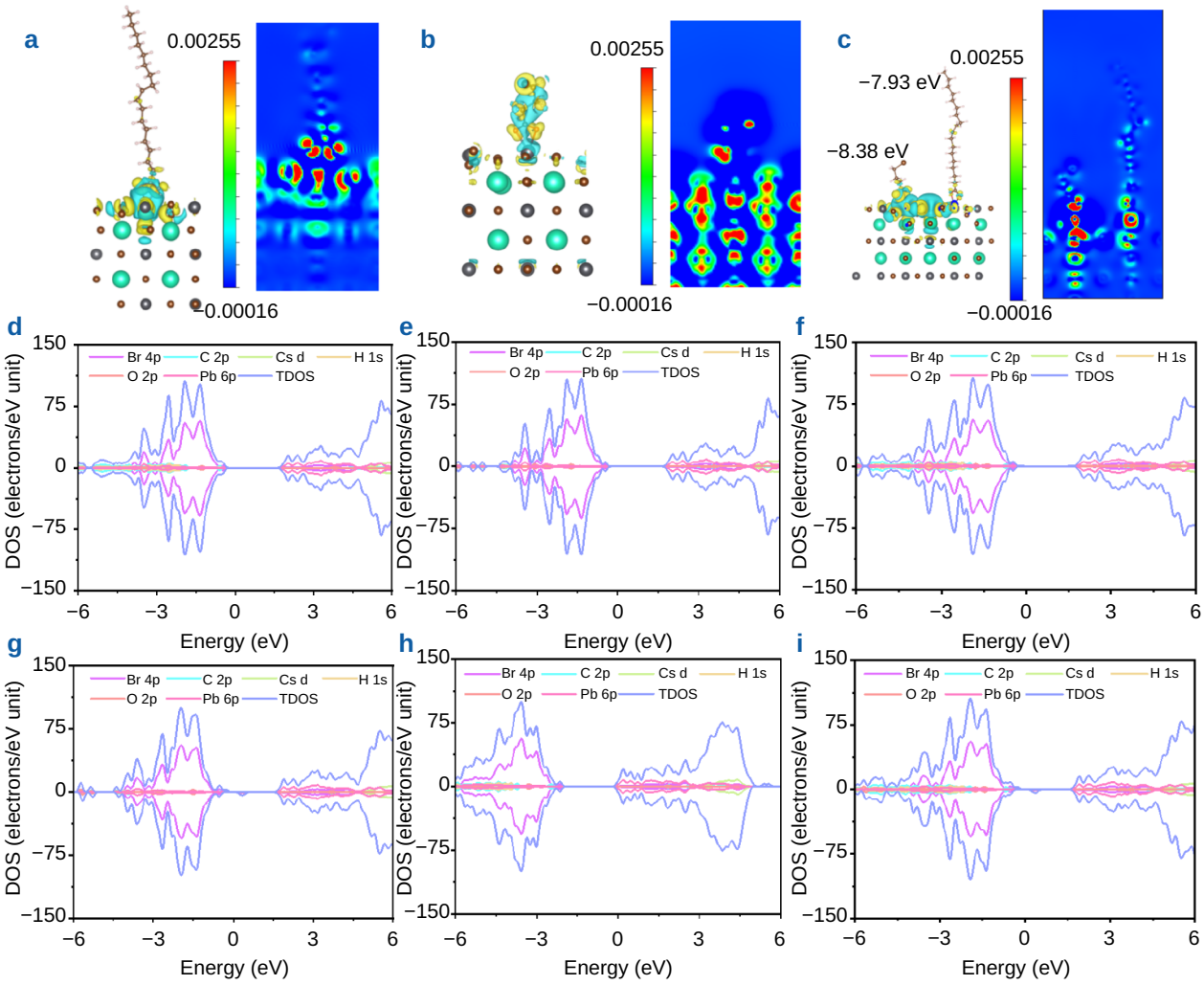


Fig. 1 | Charge density difference map of the (a) $CsPbBr_3$-OA, (b) $CsPbBr_3$-BA, (c) $CsPbBr_3$-OA/BA QDs and the bond energy of OA and BA adsorbed on $CsPbBr_3$. (d–f) The PDOS and TDOS plots of $CsPbBr_3$-OA, $CsPbBr_3$-BA and $CsPbBr_3$-OA/BA. (g–i) PDOS plots and TDOS plots for Br-vacancy defects.

electronic structure and defect tolerance of $CsPbBr_3$ QDs, we calculated the projected and total density of states (PDOS and TDOS) for $CsPbBr_3$ capped with OA, BA, OA/BA, and for the corresponding models containing a representative Br vacancy. Br vacancies were selected as a prototypical halide defect because they are widely implicated in forming deep trap states in lead halide perovskites. As shown in Fig. 1(d–f), the band-edge electronic structure is dominated by Br 4s states and Pb 6p states for all three ligand configurations, indicating that ligand adsorption does not markedly alter the intrinsic band composition. Adsorbed molecules OA, BA, and OA/BA are mainly distributed in the valence band region from −6 to 0 eV, showing significant overlap with the Br 4p orbitals, indicating orbital hybridization between the carboxyl groups of OA and BA with the perovskite surface. We then introduced a Br vacancy to evaluate defect-induced states. In $CsPbBr_3$-OA, the main peak of Br 4p extends toward deeper energy levels (−5 to −2 eV), indicating that Br vacancies cause electron cloud rearrangement of surrounding atoms. The C 2p and H 1s orbitals of OA exhibit a broad and deep overlap range with Br 4p, suggesting that the vacancies enhance the electronic interaction between OA and the surface, resulting in more stable adsorption (Fig. 1(g)). In $CsPbBr_3$-BA, the Br vacancies form stronger electrostatic/hydrogen bonding interactions with BA at the surface, leading to more significant orbital overlap and more stable adsorption. Notably, some impurity energy levels appear in the band gap, implying that Br vacancies introduce shallow acceptor states (Fig. 1(h)). In $CsPbBr_3$-OA/BA, both OA and BA are mainly distributed in the valence band region from −6 to 0 eV, and the Br vacancies significantly enhance the electronic coupling between OA and BA at the defective surface. The conduction band region (>0 eV) shows almost no contribution, indicating no gap defect states are introduced. This demonstrates that OA and BA achieve effective passivation (Fig. 1(i)). Collectively,

This is an early view version and will be formally published in a coming issue with other articles in due time.

the DOS analysis indicates that the OA/BA co-ligand configuration better mitigates vacancy-induced deep states, providing a plausible electronic-structure basis for the improved luminescence performance.

Motivated by the ligand dependent defect states revealed above, we next quantified the thermodynamic stability of halide vacancies by calculating the formation energies and Br vacancy defect formation energies for $CsPbBr_3$ capped with OA, BA, and OA/BA (Table 1). The calculation formulas are provided below:

$$E_{\text{formation}} = E_{\text{perovskite+molecule}} - E_{\text{perovskite}} - E_{\text{molecule}} . \quad (1)$$

These calculations indicate that $CsPbBr_3$ QDs capped with OA or BA alone are thermodynamically less stable, whereas co-adsorption of OA and BA substantially enhances structural stability. Under Br-vacancy conditions, the results remain consistent with those obtained for the perfect crystal. The formation energy of $CsPbBr_3$–OA/BA is lower than that of both $CsPbBr_3$–OA and $CsPbBr_3$–BA, indicating that $CsPbBr_3$–OA/BA is more stable than the latter two. Moreover, the formation energies of ligand-adsorbed $CsPbBr_3$ structures containing vacancies are generally lower than those of ligand-adsorbed $CsPbBr_3$ in the perfect crystal, suggesting that the presence of bromine vacancies facilitates the adsorption of OA and BA onto the $CsPbBr_3$ surface (Table 1).

Table 1 | Based on density functional theory (DFT) calculations, the formation energies of $CsPbBr_3$-OA, $CsPbBr_3$-BA, and $CsPbBr_3$-OA/BA systems, along with the formation energies of bromide ion vacancy defects, were systematically investigated.

Crystal	Formation energy (eV)
$CsPbBr_3$-OA	−0.039
Bromine vacancy defects in $CsPbBr_3$-OA	−0.478
$CsPbBr_3$-BA	−0.383
Bromine vacancy defects in $CsPbBr_3$-BA	−1.759
$CsPbBr_3$-OA/BA	−0.774
Bromine vacancy defects in $CsPbBr_3$-OA/BA	−2.223

Motivated by the optical performance enhancement under OA and BA co-passivation, we examined the morphology and crystallinity of $CsPbBr_3$ QDs capped with OA and with OA and BA (Fig. 2). These two samples were selected to directly correlate the ligand environment with structural metrics at the single-particle level. As shown in Fig. 2(a), TEM images of $CsPbBr_3$-OA QDs reveal uniform cubic QDs. Additionally, we measured the sizes of 72 QDs, which exhibited an average size of (19.07 ± 5.45) nm (Fig. S3(a)). The corresponding selected-area electron diffraction (SAED) pattern (inset of Fig. 2(a)) displays well-defined diffraction rings consistent with the cubic phase, and

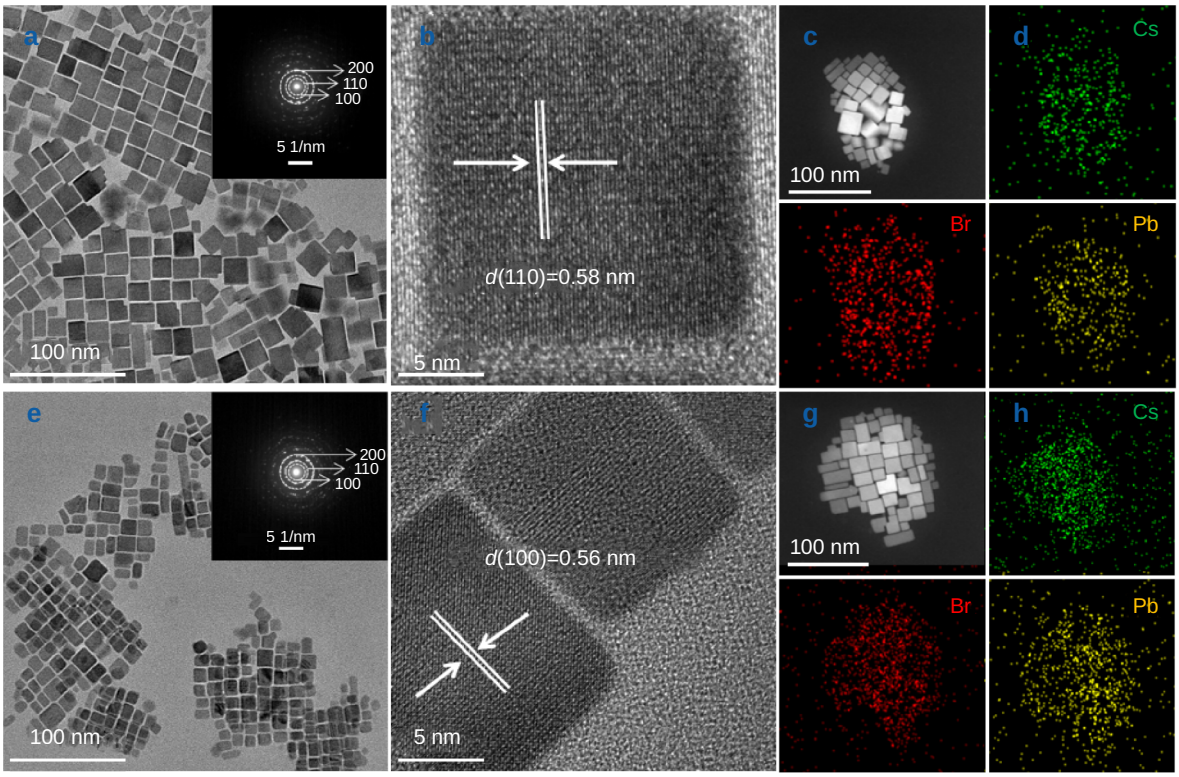


Fig. 2 | (a) The TEM image, (b) HRTEM image, (c) HAADF-STEM image and (d) mapping in $CsPbBr_3$-OA. (e) The TEM image, (f) HRTEM image, (g) HAADF-STEM image and (h) mapping in $CsPbBr_3$-OA/BA.

This is an early view version and will be formally published in a coming issue with other articles in due time.

High-resolution transmission electron microscopy (HRTEM) further confirms the single-crystalline nature of individual QDs by clear lattice fringes. A lattice d-spacing of 0.58 nm is resolved (Fig. 2(b)), assignable to the (110) planes of the cubic $CsPbBr_3$. High-angle annular dark-field scanning transmission electron microscopy (HAADF-STEM) imaging (Fig. 2(c)) and energy-dispersive X-ray (EDX) elemental mapping (Fig. 2(d)) reveal homogeneous distributions of Cs, Pb, and Br across the QDs, indicating compositional uniformity. For $CsPbBr_3$-OA/BA QDs, the particles retain a similar cubic morphology. Notably, we statistically analyzed the sizes of 78 QDs, and the average size decreased to 13.55 ± 2.94 nm. (Figs. 2(e) and S3(b)). This size reduction is consistent with ligand-dependent growth regulation and possible surface etching induced by BA. The SAED pattern again confirms the cubic lattice, indicating that BA incorporation does not alter the crystalline phase. In HRTEM, $CsPbBr_3$-OA/BA QDs show well-resolved fringes with a slightly smaller d-spacing of 0.56 nm (Fig. 2(f)), suggesting a modest lattice contraction relative to the OA-capped counterpart. This trend is consistent with the subtle peak shifts observed in XRD for BA-containing samples. HAADF-STEM and elemental mapping further confirm the spatially uniform distribution of Cs, Pb, and Br (Fig. 2(g) and 2(h)), supporting the structural and compositional homogeneity of the co-passivated QDs.

The experimental protocol is illustrated in Fig. 3(a). Perovskite precursors were dissolved in DMF together with OA, OAm, and BA, and the resulting solution was rapidly introduced into toluene. The instantaneous miscibility between DMF and toluene triggers an abrupt reduction in the solubility of Cs^+, Pb^{2+}, and Br^- species, thereby driving

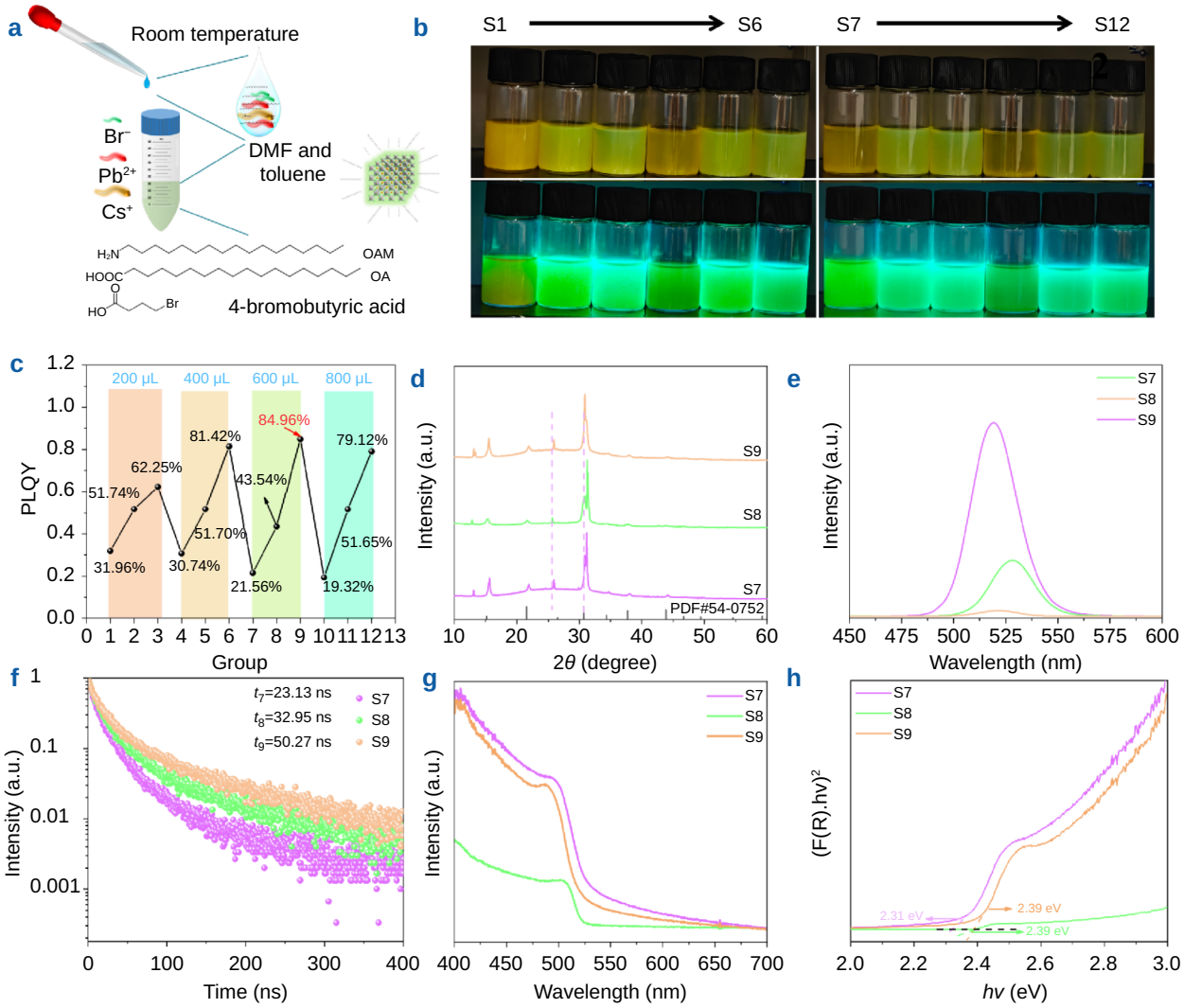


Fig. 3 | (a) Schematic diagram of the direct synthesis process of $CsPbBr_3$ QDs. (b) Images of $CsPbBr_3$ QDs prepared with different ligand ratios under natural light and 365 nm UV irradiation. (c) PLQY of $CsPbBr_3$ QDs synthesized under varied conditions. (d) XRD patterns, (e) PL spectra, (f) fluorescence lifetimes, (g) absorption spectra, and (h) Tauc plot of samples S7–S9.

This is an early view version and will be formally published in a coming issue with other articles in due time.

rapid supersaturation and homogeneous nucleation of $CsPbBr_3$ QDs. This miscibility driven route enables room temperature synthesis under ambient conditions. Using this approach, we prepared 12 QDs batches by systematically varying the ligand ratios (Table 2). Under daylight the dispersions appear yellow, while bright green emission is observed under 365 nm UV illumination, with sample S9 showing the strongest emission (Fig. 3(b)).

Table 2 | $CsPbBr_3$ QDs prepared with varying amounts of OA and BA.

Group	OAm (μL)	OA (μL)	BA (μL)
1	200	200	0
2	200	0	200
3	200	100	100
4	200	400	0
5	200	0	400
6	200	200	200
7	200	600	0
8	200	0	600
9	200	300	300
10	200	800	0
11	200	0	800
12	200	400	400

We then quantified the PLQY for S1 to S12. When the amount of OAm amount was held constant, QDs capped with OA alone or BA alone exhibit comparatively low PLQY. In contrast, co-passivation using OA and BA produces a pronounced enhancement, reaching a maximum PLQY of 84.96% at an OA to BA ratio of 1:1, corresponding to S9. (Fig. 3(c)). The presence of a distinct optimum indicates that effective passivation requires a balanced ligand environment rather than increasing a single ligand component. This trend is consistent with cooperative surface stabilization that suppresses defect assisted nonradiative recombination. XRD patterns confirm the cubic $CsPbBr_3$ phase for all samples (PDF#54-0752), indicating that BA incorporation does not induce a phase transition (Fig. S4)[22]. Notably, S9 exhibits sharper and more intense reflections than S7 and S8 (Fig. 3(d)), consistent with improved crystallinity under the optimized OA and BA condition. A subtle shift of the diffraction peaks toward higher angles is also observed upon BA incorporation.

Consistently, all samples show a dominant excitonic emission band at 510 to 530 nm (Figs. 3(e) and S5). Co-passivated QDs display enhanced emission intensity, whereas BA only samples exhibit a modest blue shift, which is consistent with increased effective confinement associated with a reduced QDs size under stronger surface etching. To further probe recombination kinetics, time resolved PL decays were collected and all fluorescence decay curves were fitted with a double exponential decay model, allowing for the extraction of both fast and slow decay lifetimes. The fitting formula is as follows[23]:

$$I(t) = A_1\exp(t_1/\tau_1) + A_2\exp(t_2/\tau_2)\ . \tag{2}$$

The average lifetime of QDs is extracted by fitting their fast and slow decay curve with the following formula[24]:

$$\tau_{ave} = \frac{A_1\tau_1^2 + A_2\tau_2^2}{A_1\tau_1 + A_2\tau_2}\ . \tag{3}$$

Figure S6 fitted with a biexponential function containing a fast component (τ_1) and a slow component (τ_2), from which the average lifetime (τ_{ave}) was obtained. The fast decay (τ_1) is associated with trap mediated recombination, whereas the slow component reflects radiative recombination. As shown in Fig. 3(f), the average lifetimes of $CsPbBr_3$ QDs capped with OA, BA, and OA/BA are 23.13, 32.95, and 50.27 ns, respectively, indicating substantially suppressed defect assisted nonradiative pathways under OA and BA co-passivation. The absorption spectra correlate well with the emission behavior, showing a pronounced absorption band around 500 to 520 nm. Upon BA incorporation, a discernible blue shift is observed. Tauc analysis further reveals a bandgap increase from 2.39 to 2.31 eV (Figs. S7, 3(g) and 3(h)), consistent with the spectral shift[25].

We also employed ^{1}H NMR spectroscopy to investigate the ligands bound to the surface of $CsPbBr_3$ QDs. In the ^{1}H NMR spectrum of $CsPbBr_3$-OA (Fig. 4(a)), distinct resonances at 5.37, 4.01, 2.74 and 2.25 ppm correspond to the C9 (C10), C1, C11, and amine protons of OAm, respectively. The peak at 8.03 ppm is assigned to the COOH proton of OA ligand. These signals confirm the presence of both OA and OAm as surface ligands on the $CsPbBr_3$ QDs. For $CsPbBr_3$-OA/BA, three additional peaks at 4.35, 3.05 and 2.53 ppm were observed, which correspond to the methylene protons of BA bound to the QDs surface[26]. These findings confirm that the surface of $CsPbBr_3$-OA/BA QDs is primarily passivated by BA ligands coordinated to Pb^{2+}, consistent with previous reports[27]. Consequently, BA plays a dominant role in stabilizing $CsPbBr_3$ QDs, with a minor contribution from OAm, leading to enhanced surface passivation. To corroborate these findings, we performed FT–IR spectroscopy, as shown in Fig. 4(b). The C–H stretching vibrations at 2851 and 2922 cm^{-1}, along with the intense C–H bending mode at 1458 cm^{-1}, correspond to the alkyl chains of BA and OAm. The band at 1638 cm^{-1} is associated with the C=O stretching vibration of carboxyl groups, while the peak at 473 cm^{-1} corresponds to the C–Br vibration of BA. These features provide additional evidence that BA's carboxyl and groups coordinate with Pb^{2+}, while OA and OAm bind Br^-, effectively passivating the $CsPbBr_3$ QDs surface and mitigating degradation in polar solvents[27].

We also conducted X-ray photoelectron spectroscopy (XPS) to further analyze their surface composition of $CsPbBr_3$-OA, $CsPbBr_3$-BA and $CsPbBr_3$-OA/BA QDs.

This is an early view version and will be formally published in a coming issue with other articles in due time.

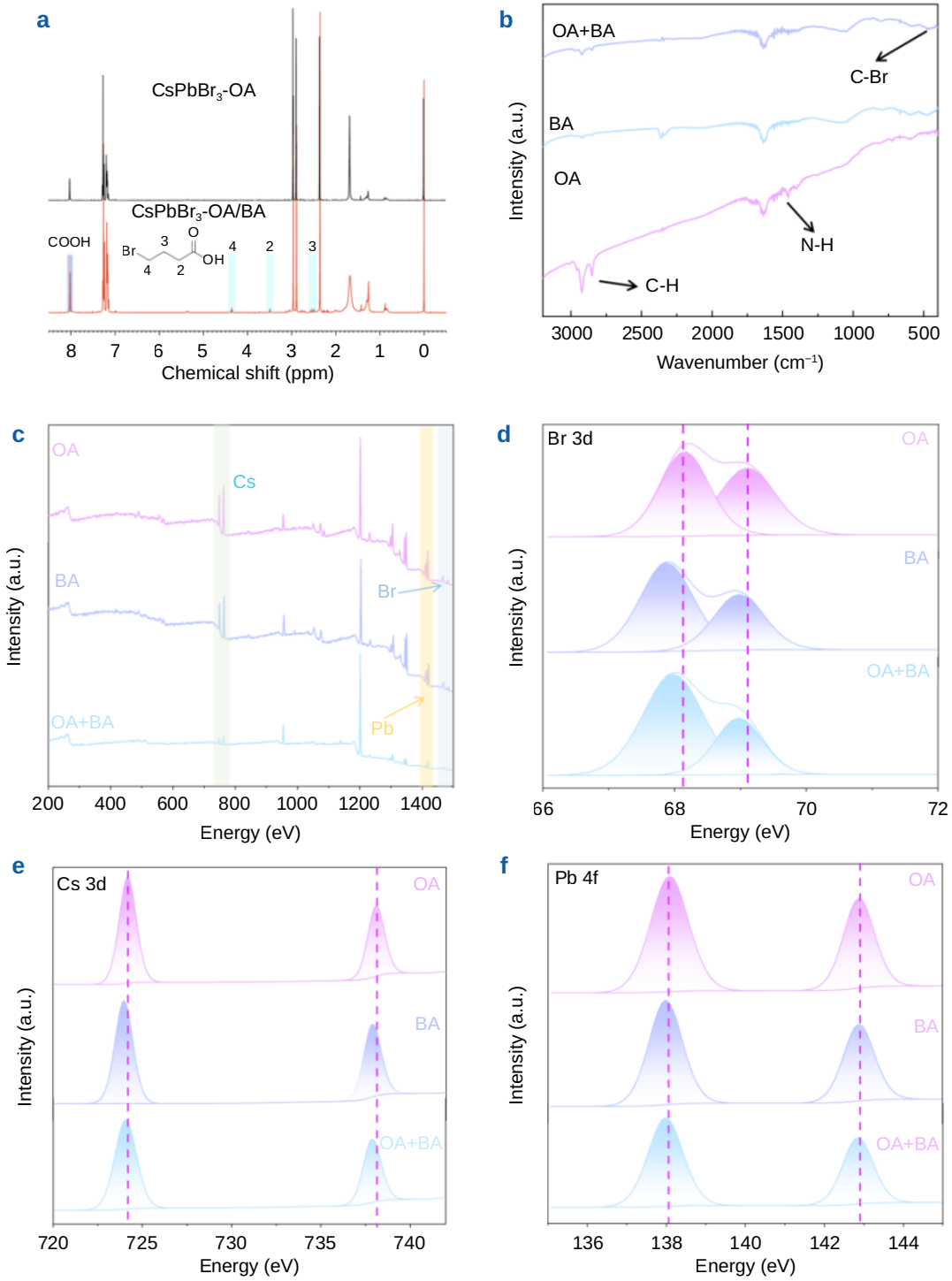


Fig. 4 | (a)^{1}H NMR spectra of $CsPbBr_3$-OA and $CsPbBr_3$-OA/BA, (b) FTIR spectra of $CsPbBr_3$-OA, $CsPbBr_3$-BA, and $CsPbBr_3$-OA/BA, (c) XPS survey spectra, and (d–f) high-resolution XPS spectra of Br, Cs, and Pb.

Figure 4(c) presents the survey spectra, where peaks corresponding to Cs, Pb and Br are clearly resolved. In the Br 3d region of $CsPbBr_3$-OA, two components centered at 69.08 eV and 68.16 eV are observed. Upon incorporation of BA, the Br 3d doublet shifts to higher binding energy (Fig. 4(d)). This could be attributed to the terminal Br of BA filling Br vacancies to restore the halide shell, thereby inducing interfacial charge transfer[10]. This process reduces trap depths and suppresses nonradiative recombination, leading to a significant increase in PLQY and prolonged fluorescence lifetime; meanwhile, it enhances structural integrity and environmental isolation, thereby improving long-term stability. Similar

This is an early view version and will be formally published in a coming issue with other articles in due time.

shifts are observed in the Cs and Pb core-level spectra, which can be attributed to lattice contraction induced by BA incorporation, modifying the local electronic environment surrounding the Pb^{2+} (Fig. 4(e) and 4(f))[10]. This indicates that BA modification has a significant effect on the surface chemical bonding characteristics of $CsPbBr_3$ QDs, thereby enhancing their optical stability.

In addition, we measured the temperature-dependent PL spectra of $CsPbBr_3$-OA and $CsPbBr_3$-OA/BA QDs over a temperature range of 77–297 K. As the temperature increased, the emission peaks of both QDs systems showed a continuous blue shift, which can be attributed to thermal expansion and dynamic octahedral tilting weaken the Pb–Br antibonding orbital overlap, thereby lowering the energy of the antibonding valence band maximum (VBM), while the conduction band minimum (CBM) remains essentially unchanged. (Fig. 5(a) and 5(c))[28,29]. Simultaneously, the PL linewidths broaden with increasing temperature, primarily due to strengthened electron-phonon coupling. The PL intensity of both $CsPbBr_3$-OA and $CsPbBr_3$-OA/BA QDs decreased progressively with increasing temperature. This thermal quenching behavior is mainly attributed to the increased phonon population at elevated temperatures, which promotes non-radiative recombination through enhanced electron–phonon scattering, as well as to the thermal activation of excitons, which facilitates their dissociation and reduces the probability of radiative recombination. To quantitatively analyze the thermal quenching process, the temperature-dependent PL intensities were subsequently fitted using the Arrhenius equation[30,31]:

$$I(t) = \frac{I_0}{1 + Ae^{-E_b/k_B T}}, \tag{4}$$

where I_0 denotes the PL intensity at 0 K, k_B is the Boltzmann constant, A is a constant, and E_b represents the exciton binding energy[32]. As illustrated in Fig. 5(b) and 5(d), the exciton binding energy is 50.09 meV for $CsPbBr_3$-OA, while it is slightly higher at 56.13 meV for the $CsPbBr_3$-OA/BA QDs. This difference arises because the Br^- ions in BA fill the Br^- vacancies within $CsPbBr_3$ QDs, thereby improving their stability and enhancing the efficiency of radiative transitions.

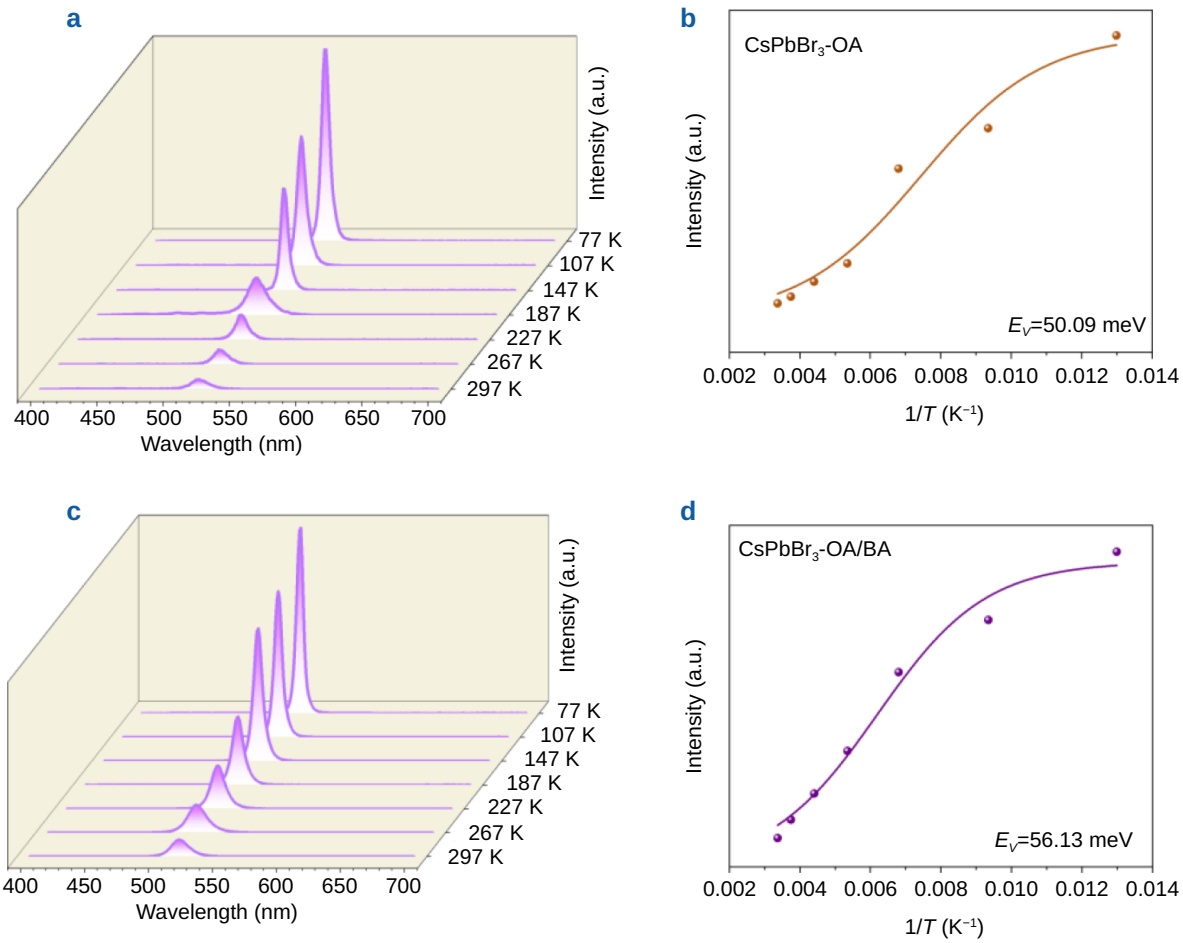


Fig. 5 | Temperature-dependent PL spectra for (a) $CsPbBr_3$-OA and (c) $CsPbBr_3$-OA/BA QDs. The extracted exciton binding energies of (b) $CsPbBr_3$-OA, (d) $CsPbBr_3$/-OA/BA QDs.

This is an early view version and will be formally published in a coming issue with other articles in due time.

We systematically investigated the fluorescence spectral properties of individual QDs under 395 nm ultraviolet excitation. Specifically, UV excitation promotes electrons from the valence band (VB) to the conduction band (CB), generating electron–hole pairs (e^-/h^+). After relaxation to the band edge, radiative recombination produces fluorescence with an emission energy mainly determined by the bandgap energy (E_g). The sample was excited at a single wavelength and the fluorescence emission signal was collected; the corresponding fluorescence spectrum was obtained by converting the time-domain signal to the frequency domain via Fourier transformation, as illustrated in the inset of Fig. 6(a). The measurements were performed using a custom-built spectral imaging dark-field microscope, the setup is depicted in the inset of Fig. 6(b). In brief, n-octane was introduced into a home-designed flow cell as the dispersion medium, followed by the injection of a diluted QDs solution. This procedure allowed for the uniform deposition of individual QDs onto a glass substrate. Fluorescence spectra of single particles were subsequently acquired through point-by-point scanning using a hyperspectral camera, providing representative spectra of individual QDs, as shown in Fig. 6(b). These spectra were fitted with a Lorentzian function, and the resonance energy was extracted to be approximately 2.4 eV, with a corresponding FWHM of approximately 84 meV. Using the relationship between the homogeneous linewidth and the dephasing time, $T \cdot FWHM = 2\hbar$[33], we determined the dephasing time of the individual QDs. As shown in Fig. 6(c) and 6(d), consistent decreasing trends are observed for individual QDs across three independent experiments, demonstrating the improved statistical reliability of the results. The single-particle distributions reveal that the FWHM values before and after modification are relatively narrow, suggesting good sample uniformity at the single-particle level. This reflects the stability and reproducibility of the QDs synthesis process. As shown in Fig. 6(e), a comparison of the average FWHM between $CsPbBr_3$-OA QDs (89.48 meV) and $CsPbBr_3$-OA/BA QDs (82.47 meV) after modification reveals a clear narrowing of the linewidth, this indicates that BA not only improves the performance of the ensemble, but also fundamentally reduces the inhomogeneity and spectral diffusion of each particle. This means that the surface charge environment becomes more stable, and the exciton-phonon coupling is weakened. Although some individual data points show partial overlap of the error bars, the consistent trend across all three independent measurements clearly indicates that BA ligand significantly reduces the homogeneous linewidth of the QDs (Fig. S8).

Furthermore, the dephasing times derived from the

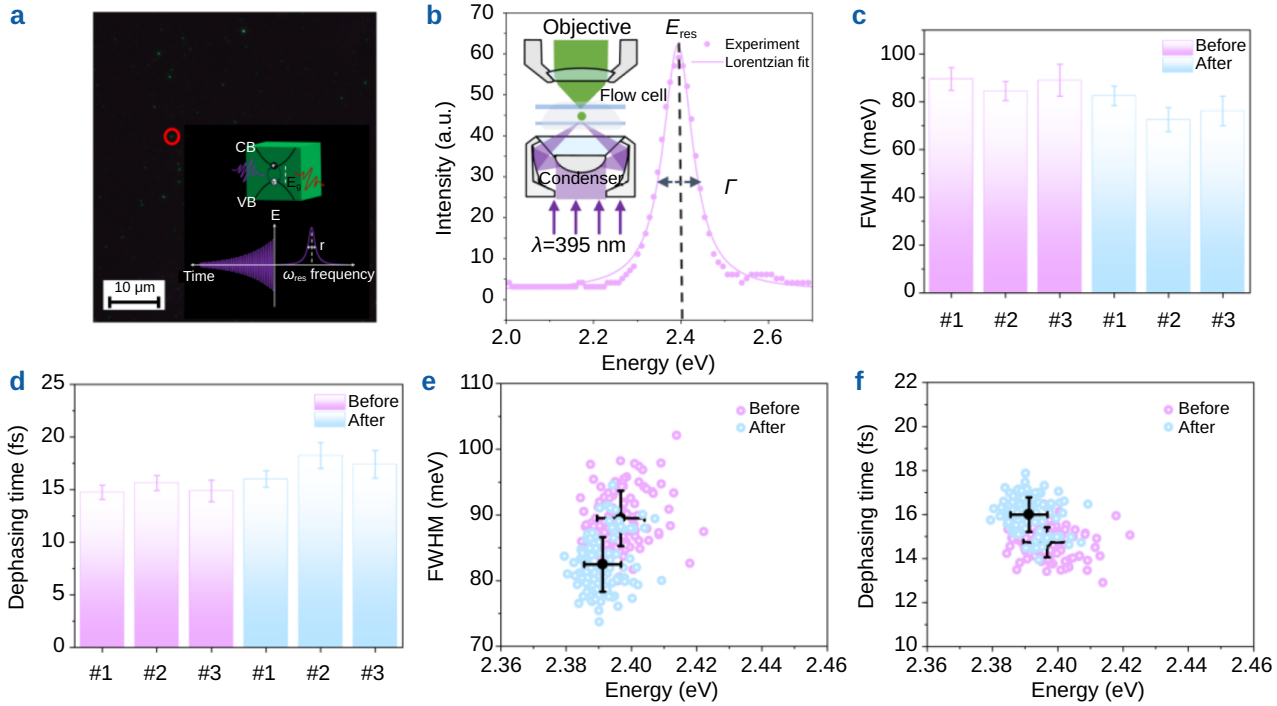


Fig. 6 | (a) Single-particle dark-field fluorescence image of QDs. Inset: Schematic illustration of the fluorescence mechanism and the time–frequency domain transformation. (b) Representative single particle dark-field fluorescence spectra of QDs for linewidth (Γ) extraction. Inset: Optical configuration of the dark-field microscopy system. (c–d) FWHM and dephasing time from three independent experiments (labeled 1–3) for $CsPbBr_3$ QDs (purple) and $CsPbBr_3$-OA QDs (light blue). (e–f) The FWHM and dephasing time of 112 individual $CsPbBr_3$-OA QDs (purple) and 104 $CsPbBr_3$-OA/BA QDs (light blue), respectively.

This is an early view version and will be formally published in a coming issue with other articles in due time.

FWHM values are presented in Fig. 6(f). The average dephasing time of $CsPbBr_3$-OA/BA QDs increases from approximately 14.74 fs to 16.00 fs, exhibiting a trend opposite to that of the FWHM. These results suggest that BA ligand not only reduces homogeneous broadening but also substantially extends the exciton dephasing time, indicating enhanced excitonic coherence. This improvement is mainly attributed to the passivation of surface trap states and the suppression of local environmental fluctuations, which jointly stabilize the excitonic state and provide important support and potential for the application of QDs in the field of quantum optics[34,35].

We further evaluated the photostability, water stability, and thermal stability of the PL of $CsPbBr_3$-OA and $CsPbBr_3$-OA/BA QDs. Both samples were dispersed in n-octane and subsequently mixed with water at a 1:1 volume ratio in a cuvette, and the PL intensity was monitored at hourly intervals. For $CsPbBr_3$-OA QDs, the PL intensity decreased rapidly upon water exposure, dropping to 21% of its initial value after 3 h. A gradual red-shift in the PL peak was observed, which can be attributed to QDs aggregation caused by partial ligand desorption and subsequent degradation in the aqueous environment. By contrast, $CsPbBr_3$-OA/BA QDs exhibited significantly enhanced water stability, retaining 81% of their initial PL intensity after 3 h, demonstrating that BA effectively suppresses QDs dissociation and aggregation in water (Figs. 7(a–c), S8(a–d)).

The photostability of the QDs was further assessed under continuous ultraviolet irradiation. $CsPbBr_3$-OA and $CsPbBr_3$-OA/BA QDs samples were exposed to 1200 mW cm^{-2} UV lamp for 3 h. Under intense UV irradiation, the emission intensity of $CsPbBr_3$-OA QDs rapidly diminished and exhibited a pronounced red shift, with the emission being nearly completely quenched after 3 h. This severe degradation is ascribed to ligand detachment under photoexcitation, which promotes QDs aggregation. Consistent with this interpretation, visible precipitation was observed after prolonged irradiation. In contrast, $CsPbBr_3$-OA/BA QDs exhibited stable emission, preserving 88% of their initial PL intensity after the same 3 h of UV exposure (Figs. 7(d–f), S9(a–d)). The thermal stability of $CsPbBr_3$-OA and $CsPbBr_3$-OA/BA QDs is shown in Fig. S10. As temperature increased, thermally activated lattice vibrations led to significant PL quenching in both samples. Notably, OA/BA-capped $CsPbBr_3$ QDs displayed improved thermal stability compared to their OA-capped counterparts, consistent with more effective surface passivation that reduces thermally induced non-radiative recombination.

To further explore the potential applications of $CsPbBr_3$-OA and $CsPbBr_3$-OA/BA QDs in green-light LED devices, we examined their thermal stability and operational performance. All LED fabrication steps were carried out under ambient conditions. $CsPbBr_3$-OA and $CsPbBr_3$-OA/BA QDs were integrated with 365 nm chips by mixing them with

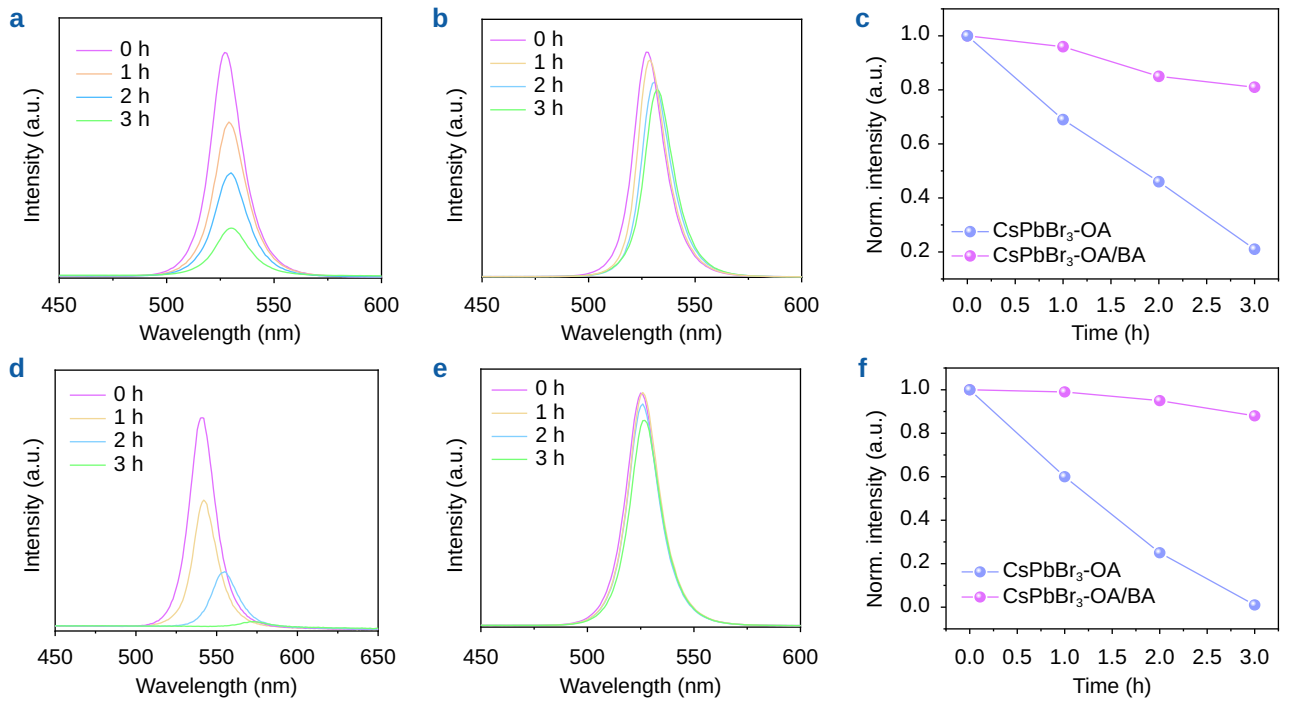


Fig. 7 | PL spectra of (a) $CsPbBr_3$-OA and (b) $CsPbBr_3$-OA/BA under the influence of water at different time intervals, along with (c) the corresponding decay line chart. PL spectra of (d) $CsPbBr_3$-OA and (e) $CsPbBr_3$-OA/BA under UV illumination at different time intervals, along with (f) the corresponding decay line chart.

This is an early view version and will be formally published in a coming issue with other articles in due time.

PMMA in toluene. At a driving voltage of 2.25 V, the LED based on pure $CsPbBr_3$-OA QDs emitted green light with a peak at approximately 560 nm (Fig. 8(a)). In contrast, the LED fabricated with $CsPbBr_3$-OA/BA QDs emitted at approximately 540 nm, exhibiting not only higher intensity but also a narrower FWHM compared to the $CsPbBr_3$-OA counterpart. The inset of Fig. 8(a) illustrates that the LED fabricated from $CsPbBr_3$-OA/BA QDs emits noticeably brighter green light. The CIE chromaticity coordinates for the LEDs based on $CsPbBr_3$-OA and $CsPbBr_3$-OA/BA are (0.32, 0.66) and (0.39, 0.56), respectively, as shown in Fig. 8(b). Notably, the emission wavelength of the LED device exhibits a significant red-shift compared to that of the $CsPbBr_3$ QDs solution, which may be attributed to severe self-absorption and electron wavefunction overlap occurring after the $CsPbBr_3$ is processed into a thin film[36,37]. The PL spectra of $CsPbBr_3$-OA and $CsPbBr_3$-OA/BA QDs on 365 nm chips at various applied voltages are shown in Fig. 8(c) and 8(d). As the voltage increases from 2.55 to 2.85 V, the emission intensities of both LEDs increase. Over this voltage range, the device incorporating $CsPbBr_3$-OA/BA QDs consistently exhibits higher emission intensity and EQE than its $CsPbBr_3$-OA counterpart. Notably, the $CsPbBr_3$-OA/BA-based LED achieves an EQE of 2.25 % at 2.65 V, highlighting its superior potential for future applications (Fig. 8(e) and 8(f)).

Table 3 compares the PLQY of $CsPbBr_3$-OA/BA and the EQE of the fabricated LEDs with previously reported values, demonstrating that this work achieves above-average performance in both luminescence properties and device fabrication, thereby highlighting its considerable potential for future practical applications. Additionally, the LED based on $CsPbBr_3$-OA shows a slight shift in its emission peak as the applied voltage increases, whereas the device with $CsPbBr_3$-OA/BA exhibits minimal change in emission center. This shift is likely due to the increased temperature of the 365 nm UV chip at higher voltages. To investigate this further, real-time infrared thermography was used to monitor the temperature of the commercial 365 nm UV chip at various voltages (Fig. 8(g)). The results reveal that the chip temperature increases from 28.3 °C to 51.8 °C as the voltage rises from 2.55 V to 2.85 V, further demonstrating the superior thermal stability of the LED incorporating $CsPbBr_3$-OA/BA QDs.

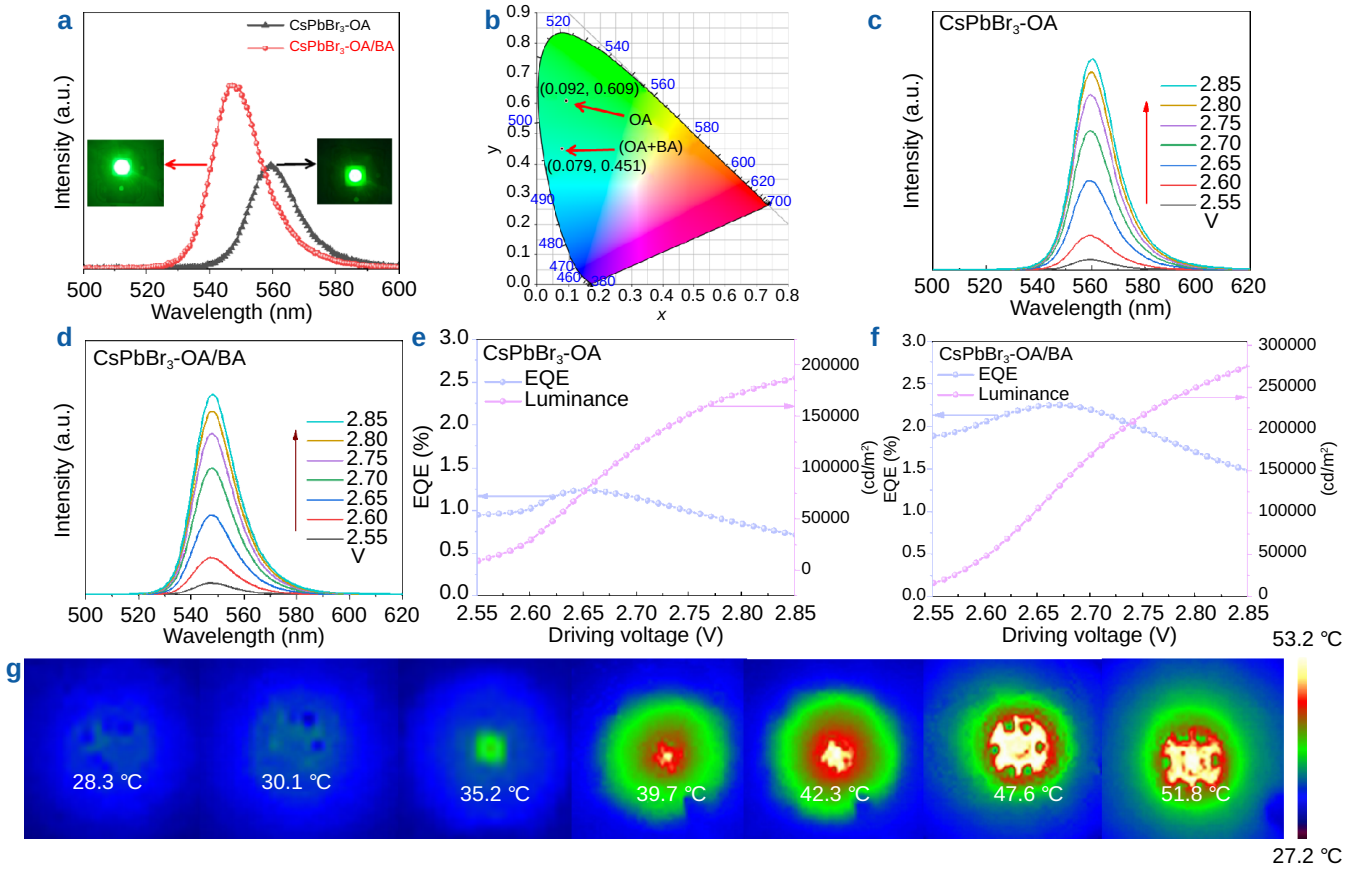


Fig. 8 | (a) PL intensity spectra and (b) CIE chromaticity coordinates of the green LEDs fabricated by coupling $CsPbBr_3$-OA and $CsPbBr_3$-OA/BA with a commercial 365 nm chip. (c–d) PL intensity, (e-f) EQE and luminance of $CsPbBr_3$-OA and $CsPbBr_3$-OA/BA devices measured under various applied voltages. (g) Variation of the actual temperature for the commercial UV LED chip with the increase of the forward bias voltage.

This is an early view version and will be formally published in a coming issue with other articles in due time.

Table 3 | Comparison of PLQY and fabricated LED performance of different fluorescent materials

Chemical formula	Emission peak (nm)	Synthesis method	EQE (%)	PLQY (%)	Ref
$Cs_3Cu_2Cl_5$: Mg^{2+}	541	Hot-injection	0.173	59.30	ref.[38]
$CsPbCl_3$:Yb^{3+}	1000	Hot-injection	2	110	ref.[39]
$CsPbBr_3$:Ce^{3+}	510	Supersaturation recrystallization	4.8	89	ref.[40]
$Cs_3Cu_2Cl_5$:Rb^{+}	462	Solvent evaporation	0.254	98.72	ref.[41]
$CsPbBr_3$@KBr	524	Cold sintering process	/	73.6	ref.[42]
$CsPbI_3$:Mg^{2+}	650	Hot-injection	11.87	42	ref.[43]
$CsPbBr_3$-OA/BA	540	Supersaturation recrystallization	2.65	84.96	This work

3 Conclusion

In summary, we achieved the efficient and stable synthesis of $CsPbBr_3$ QDs at room temperature by introducing a short-chain bifunctional ligand BA, attaining a PLQY of 84.96%. By coupling with a 365 nm UV chip, we fabricated LEDs with an external quantum efficiency (EQE) of 2.25%. Combined DFT calculations and single-particle dark-field spectroscopy show that BA strengthens surface binding and passivates vacancy-related defects, thereby narrowing the emission linewidth and enhancing excitonic coherence in individual QDs. This work demonstrates that finely designing the molecular structure of ligands (chain length, terminal functional groups) to regulate the electronic structure and chemical environment of QDs surfaces is a universal strategy for achieving high-performance and high-stability optoelectronic devices, and opens new possibilities for the application of perovskite QDs in optoelectronic and other fields.

4 Experimental section

Chemicals: lead bromide ($PbBr_2$, 99.9%, Adamas), cesium bromide (CsBr, 99.9%, Adamas), oleic acid (OA, >90%, Adamas), oleylamine (OAm, >90%, Adamas), 4-Bromobutyric acid (BA, 98%), N,N-Dimethylformamide (DMF, 99%), methylbenzene, normal octane (95%, Meryer), Polymethyl methacrylate (PMMA,99%, ALDRICH)

Preparation of the precursor solution: Mixed 147 mg of lead bromide and 85.2 mg of cesium bromide powders with 10 mL of DMF in a glass vial. Placed a magnetic stired bar into the vial and set it on a rotating platform. Stir at 500 RPM until the solution becomes clear and transparent. Then OAm, OA, and BA were added in different proportions, heated to 40 °C and stirred for 15 minutes until the mixture became clear and transparent.

Preparation of $CsPbBr_3$ QDs: Transferred 20 mL of toluene into a centrifuge tube and placed it on a rotary platform; adjusted the speed until a vortex formed in the toluene. Quickly injected 1 mL of the precursor solution into the toluene, and crystalline precipitate immediately began to appear. Increased the rotation speed until the reaction reached equilibrium. Finally, added ethyl acetate to the resulting mixture and centrifuged; the precipitate was $CsPbBr_3$ QDs. Stored the sample in normal octane.

Characterization: The morphology of samples was characterized by an optical camera (D750, Nikon, Japan), transmission electron microscopy (TEM, JEOL-2100F, Japan). The structural and electronic properties of samples were characterized by X-ray diffraction patterns (XRD, Thermo ARL X'TRA, Switzerland), X-ray photoelectron spectroscopy (XPS, Ulvac-Phi, Inc., Japan). The performance of LEDs was evaluated with a commercial system (XPQY-EQE, Guangzhou Xi Pu Optoelectronics Technology Co., Ltd). The PLQY and lifetime measurements were conducted using an Edinburgh FLS1000 spectrometer. Absorption spectra were acquired using an Ocean Optics Maya2000 Pro spectrophotometer. Hydrogen nuclear magnetic resonance (^{1}H NMR) spectra were recorded on a Bruker AVANCE Il 400 MHz spectrometer (Bruker, Germany).

DFT calculation: All the calculations are performed in the framework of the density functional theory with the projector augmented plane-wave method, as implemented in the Vienna ab initio simulation package[44]. The generalized gradient approximation proposed by Perdew, Burke, and Ernzerh of is selected for the exchange-correlation potential[45]. The long-range van der Waals interaction is described by the DFT-D2 approach[46]. The cut-off energy for plane wave is set to 500 eV. The energy criterion is set to 10^{-5} eV in iterative solution of the Kohn-Sham equation. The Brillouin zone integration is performed using a 5×5×1, 3×3×1 k-mesh. All the structures are relaxed until the residual forces on the atoms have declined to less than −0.02 eV/Å.

Single particle: A custom-built spectral imaging dark-field microscope was utilized for statistically robust characterization of fluorescence property in individual QDs through homogeneous linewidth analysis. The system, constructed on a Zeiss Axioscope 5 upright microscope platform, integrated with a 395 nm ultraviolet light source and a hyperspectral camera for spectroscopic detection. Dark-field illumination was achieved via an oil-immersion condenser (NA 1.2-1.4), while dual objectives provided flexible imaging modalities: an EC-Epiplan 50×/0.75 dry objective for rapid particle localization and a Plan-Apochromat 63×/1.4

This is an early view version and will be formally published in a coming issue with other articles in due time.

oil-immersion objective for high-resolution spectral acquisition. Fluorescence from QDs with 395 nm was resolved with homogeneous linewidths (FWHM) extracted through Lorentzian fitting.

Flow cell device: The single-particle experiments employed custom-fabricated microfluidic cells constructed through a thermal lamination protocol. A dual-coverslip architecture was implemented using two glass coverslips separated by a paraffin film spacer (Parafilm M) patterned with microchannels. The assembly process involved precise alignment of access ports (1 mm diameter) drilled in the coverslips with channel termini, followed by thermal bonding at 120 °C for 15–20 seconds using a digital heating plate.

References

1. Xu N, Qi XR, Shen ZQ et al. Point defects in metal halide perovskites. *Nat Rev Phys* **7**, 554–564 (2025).
2. Ma H, Ahn E, Lee D et al. Water-induced degradation mechanism of metal halide perovskite nanocrystals. *Matter* **8**, 102083 (2025).
3. Ji R, Mallick A, Rivkin B et al. Solvent-free fabrication methods of metal halide perovskites. *Adv Mater* **37**, 2416604 (2025).
4. Wu YT, Zhu HC, Huang ZG et al. Unlocking megawatt-peak-power laser emission with colloidal quantum dots. *Sci Adv* **11**, eaea8326 (2025).
5. Cao YX, Wang XC, Zheng WL et al. Discovering structure-adaptive oxides for embedded epitaxial growth of perovskite nanocrystals. *J Am Chem Soc* **148**, 5754–5763 (2026).
6. Sharma R, Zhang QN, Nguyen LL et al. Effect of air exposure on electron-beam-induced degradation of perovskite films. *ACS Nanosci Au* **3**, 230–240 (2023).
7. Ummadisingu A, Steier L, Seo JY et al. The effect of illumination on the formation of metal halide perovskite films. *Nature* **545**, 208–212 (2017).
8. Cheng T, Cheng PP, Iqbal S et al. Extreme high-temperature effects on optical response of $CsPbBr_3$ perovskite. *Appl Phys Lett* **125**, 092102 (2024).
9. Zhang XL, Huang HH, Zhao CY et al. Surface chemistry-engineered perovskite quantum dot photovoltaics. *Chem Soc Rev* **54**, 3017–3060 (2025).
10. Tian SN, Wang J, Zhao L et al. Stable red-emission mixed halide $CsPb(Br/I)_3$ perovskite quantum dots for LEDs. *Inorg Chem* **64**, 21991–22000 (2025).
11. Ye CY, Zhou YJ, Ge J et al. Mechanistic insights into the photoluminescence enhancement in surface ligand modified $CsPbBr_3$ perovskite nanocrystals. *J Phys Chem Lett* **15**, 226–233 (2024).
12. Liu ZS, Wang Y, Zhao F et al. Liquid bidentate ligand for full ligand coverage towards efficient near-infrared perovskite quantum dot LEDs. *Light Sci Appl* **14**, 35 (2025).
13. Han SH, Jeong WH, Seo G et al. Synergistic hybrid-ligand passivation of perovskite quantum dots: suppressing reduced-dimensionality and enhancing optoelectronic performance. *Adv Mater* **37**, 2410128 (2025).
14. Xiao SH, Wang JX, Mei XY et al. In situ zwitterionic ligands consolidated surface matrix of perovskite quantum dots for efficient red LEDs. *Adv Funct Mater* **36**, e14309 (2026).
15. Zeng QS, Zhang XY, Bing QM et al. Surface stabilization of colloidal perovskite nanocrystals via multi-amine chelating ligands. *ACS Energy Lett* **7**, 1963–1970 (2022).
16. Akash S, Akhil S, Sanjana V et al. Suppressing phase segregation in mixed halide $CsPbI_{3-x}Br_x$ perovskites by dual passivation using sodium dodecyl sulphate. *Sol Energy* **274**, 112596 (2024).
17. Wu XG, Jing YY, Zhong HZ. In situ fabricated perovskite quantum dots: from materials to applications. *Adv Mater* **37**, 2412276 (2025).
18. Xie MY, Li HR, Bi CH et al. Hard-soft-acid-base management enabled bright and stable pure-blue perovskite quantum dot LEDs. *ACS Nano* **19**, 28432–28440 (2025).
19. Liu C, Lin J, Zhai W et al. Solvothermal synthesis of Mn-doped $CsPbCl_3$ perovskite nanocrystals with tunable morphology and their size-dependent optical properties. *RSC Adv* **9**, 39315–39322 (2019).
20. Li XM, Wu Y, Zhang SL et al. $CsPbX_3$ quantum dots for lighting and displays: room-temperature synthesis, photoluminescence superiorities, underlying origins and white light-emitting diodes. *Adv Funct Mater* **26**, 2435–2445 (2016).
21. Sun SB, Yuan D, Xu Y et al. Ligand-mediated synthesis of shape-controlled cesium lead halide perovskite nanocrystals *via* reprecipitation process at room temperature. *ACS Nano* **10**, 3648–3657 (2016).
22. Zhang ZW, Zhang JK, Zhao YX et al. Reviving aged $CsPbBr_3$ quantum dots by triallylamine etching. *Appl Surf Sci* **612**, 155775 (2023).
23. Fang XC, Chen Z, Leung MHM et al. Photo-induced synthesis of ytterbium and manganese-doped $CsPbCl_3$ nanocrystals for visible to near-infrared photoluminescence with negative thermal quenching. *Adv Sci* **12**, 2408927 (2025).
24. Fang XC, Zheng B, Ding MY et al. Light-induced synthesis of highly stable $CsPbCl_3$: Mn^{2+}@$mSiO_2$ nanocomposites for white light-emitting diodes. *Chem Eng J* **500**, 157339 (2024).
25. Fang XC, Zheng B, Sun XL et al. Plasmon-enhanced luminescence in ytterbium-doped halide perovskite nanocrystals for versatile applications. *J Alloys Compd* **1032**, 181105 (2025).
26. Zhu H, Pan YX, Peng CD et al. 4-Bromo-butyric acid-assisted in situ passivation strategy for superstable all-inorganic halide perovskite $CsPbX_3$ quantum dots in polar media. *Angew Chem Int Ed* **61**, e202116702 (2022).
27. Yan DD, Shi TC, Zang ZG et al. Ultrastable $CsPbBr_3$ perovskite quantum dot and their enhanced amplified spontaneous emission by surface ligand modification. *Small* **15**, 1901173 (2019).
28. Cannelli O, Wiktor J, Colonna N et al. Atomic-level description of thermal fluctuations in inorganic lead halide perovskites. *J Phys Chem Lett* **13**, 3382–3391 (2022).
29. Fasahat S, Fiuza-Maneiro N, Schäfer B et al. Sign of the gap temperature dependence in $CsPb(Br, Cl)_3$ nanocrystals determined by Cs-rattler-mediated electron-phonon coupling. *J Phys Chem Lett* **16**, 1134–1141 (2025).
30. Liao HW, Zheng JX, Huang YF et al. Dual active sites based $CsPbBr_3$/porous carbon nitrides S-scheme heterojunction for synergetic vanillin and hydrogen peroxide production. *Chem Eng J* **524**, 169068 (2025).
31. Zhang J, Shen X, Ma SY et al. Temperature-dependent photoluminescence and third-order nonlinear optical properties of Mn^{2+} doped $CsPbCl_3$ nanocrystals. *Opt Mater* **136**, 113362 (2023).
32. Das A, Pradhan J, Kalita S et al. Local atomic off-centering mediated efficient self-trapped excitonic emission in $Cs_5Cu_3Cl_6I_2$ nanoplates. *Angew Chem Int Ed* **64**, e202506404 (2025).
33. Sönnichsen C, Franzl T, Wilk T et al. Drastic reduction of Plasmon damping in gold nanorods. *Phys Rev Lett* **88**, 077402 (2002).
34. Wang YT, Long R. Rapid decoherence induced by light expansion suppresses charge recombination in mixed cation perovskites: time-domain *ab initio* analysis. *J Phys Chem Lett* **11**, 1601–1608 (2020).
35. Cai R, Wadgaonkar I, Lim J W M et al. Zero-field quantum beats and spin decoherence mechanisms in $CsPbBr_3$ perovskite nanocrystals. *Nat Commun* **14**, 2472 (2023).
36. Liu Y, Li YX, Gao KM et al. Sub-single-exciton optical gain in lead halide perovskite quantum dots revealed by exciton polarization spectroscopy. *J Am Chem Soc* **145**, 25864–25873 (2023).

This is an early view version and will be formally published in a coming issue with other articles in due time.

37. Okamoto T, Biju V. Slipping-free halide perovskite supercrystals from supramolecularly-assembled nanocrystals. *Small* **19**, 2303496 (2023).
38. Tang Y, Xie QY, Zhang XM et al. Scalable open-air synthesis of Mg^{2+}-doped lead-free $Cs_3Cu_2Cl_5$ nanocrystals for high-performance green LEDs. *Laser Photonics Rev* **19**, 2500430 (2025).
39. Huang H, Li RF, Jin SL et al. Ytterbium-doped $CsPbCl_3$ quantum cutters for near-infrared light-emitting diodes. *ACS Appl Mater Interfaces* **13**, 34561–34571 (2021).
40. Yao JS, Ge J, Han BN et al. Ce^{3+}-doping to modulate photoluminescence kinetics for efficient $CsPbBr_3$ nanocrystals based light-emitting diodes. *J Am Chem Soc* **140**, 3626–3634 (2018).
41. Zhang XM, Lu RG, Fang XC et al. Efficient blue-emitting Rb^{+}-doped $Cs_3Cu_2I_5$ via solvent evaporation crystallization for white LEDs. *Adv Opt Mater* **14**, e03766 (2026).
42. Gao J, Ren Y, Ding Q et al. Cold sintering of $CsPbBr_3$ quantum dots embedded KBr ceramics for LED displays. *J Materiomics* **11**, 100933 (2025).
43. Zheng JY, Ma JW, Yu MH et al. Efficient open-air synthesis of Mg^{2+}-doped $CsPbI_3$ nanocrystals for high-performance red LEDs. *Nanoscale* **16**, 14108–14115 (2024).
44. Kresse G, Joubert D. From ultrasoft pseudopotentials to the projector augmented-wave method. *Phys Rev B* **59**, 1758–1775 (1999).
45. Perdew JP, Burke K, Ernzerhof M. Generalized gradient approximation made simple. *Phys Rev Lett* **77**, 3865–3868 (1996).
46. Grimme S, Antony J, Ehrlich S et al. A consistent and accurate *ab initio* parametrization of density functional dispersion correction (DFT-D) for the 94 elements H-Pu. *J Chem Phys* **132**, 154104 (2010).

Acknowledgements

This research was supported by the National Natural Science Foundation of China (Nos. 62475062, 62305095), the Hainan Provincial Natural Science Foundation of China (Nos. 125MS001, 124RC439, 124YXQN412, 122RC538), and Hainan Province "Nanhai New Star" Science and Technology Innovation Talent Platform Program (NHXXRCXM202304).

Author contributions

Xiaochen Fang: Writing – original draft, Investigation. Zengxian Tang: Writing – review & editing, Supervision, Conceptualization. Ronggan Lu: Data curation. Guixiang Ding: Software. Xiaotong Zhang: Validation, Investigation. Yongfeng Liu: Investigation, Data curation. Qingyu Xie: Validation, Data curation. Dongdong Yan: Validation, Data curation, writing – review & editing, Funding acquisition. Hao Xie: Writing – review & editing, Resources, Funding acquisition. Weixiang Ye: Project administration, Methodology, Funding acquisition, Conceptualization.

Competing interests

The authors declare no competing financial interests.

Open Access This article is licensed under a Creative Commons Attribution 4.0 International License, which permits use, sharing, adaptation, distribution and reproduction in any medium or format, as long as you give appropriate credit to the original author(s) and the source, provide a link to the Creative Commons license, and indicate if changes were made. To view a copy of this license, visit http://creativecommons.org/licenses/by/4.0/
©The Author(s) 2027.
Published by Editorial Office of *Opto-Electronic Technology*, Institute of Optics and Electronics, Chinese Academy of Sciences.

Opto-Electronic Journals Group
www.oejournal.org
Scan for Article PDF

This is an early view version and will be formally published in a coming issue with other articles in due time.